Interface structure of MBE-grown $CoSi_2$/Si/$CoSi_2$ layers on Si(111): Partially correlated roughness and diffuse x-ray scattering

J. Stettner, L. Schwalowsky,* O. H. Seeck, M. Tolan, and W. Press
Institut für Experimentalphysik, Christian-Albrechts-Universität Kiel, Leibnizstrasse 19, D-24098 Kiel, Federal Republic of Germany

C. Schwarz and H. v. Känel
Laboratorium für Festkörperphysik, Eidgenössische Technische Hochschule Hönggerberg, CH-8093 Zürich, Switzerland
(Received 18 April 1995)

The detailed interface structure of a $CoSi_2$/Si/$CoSi_2$/Si(111) layer system grown by molecular-beam epitaxy is investigated in this paper. Measurements of the diffuse scattering in the region of total external reflection were performed and analyzed within the distorted-wave Born approximation. The analysis of the specularly reflected and the diffusely scattered intensity leads to a consistent set of interface and layer parameters, which are compared with results of Rutherford backscattering/channeling, transmission electron microscopy, and scanning tunneling microscopy. Although the diffuse intensity is dominated by a very rough surface layer, the roughness distribution of the buried interfaces of the epitaxial layers was determined rather exactly. It was found that the roughnesses of the interfaces of all epitaxial layers are of the order of monolayer steps. Very good agreement between the measurements and the calculations is achieved, if conformal roughness of the adjacent interfaces of each $CoSi_2$ layer is included. Furthermore, the interfaces of the sandwiched Si layer are partially correlated, which means that the step structure is partially transferred through all interfaces up to the surface of the upper $CoSi_2$ layer.

I. INTRODUCTION

Knowledge of the quantities which describe the morphology of interfaces, e.g., the root-mean-square (rms) roughnesses, the lateral correlation functions, and the correlations between different interfaces, is of both practical and fundamental interest. (i) Interfacial roughness is crucial for technological applications of multilayers as x-ray mirrors. Roughness attenuates the specular reflectivity and vertical correlations give rise to additional diffuse scattering[1–11] which leads to a decreased resolution of these optical devices.[12] Moreover, the fabrication of devices in microelectronics demands extremely thin metallic films with high electric conductivity which is severely degraded by interfacial roughness and influenced by the autocorrelation functions of the film interfaces.[13,14] (ii) The scientific interest mainly consists in the understanding of the atomistic processes of film growth by the determination of the scaling exponents which describe the evolution of the roughness with evaporation time.[2,3,8,9,15–22]

Specular and diffuse scattering of x rays in the range of total external reflection is an excellent tool for the investigation of the mesoscopic structure of thin films and heterostructures. In particular, x-ray scattering is well suited for the detailed characterization of interface roughness. The specular reflectivity yields the density profile perpendicular to the surface averaged over the illuminated area, i.e., film thicknesses, rms roughness,[23–25] and refractive indices. The calculations of the reflectivity are based on the formalism of Parrat.[26,27] Roughness can be included into the description in a straightforward manner (see, e.g., Refs. 28–31).

In order to characterize the lateral structure of the roughness, the diffuse nonspecular intensity has to be analyzed. Several theoretical descriptions have been developed in the past. Within the Born approximation (BA) multiple scattering, extinction and refraction effects are neglected. Therefore kinematical models are only valid for large incidence and exit angles α_i and α_f, respectively. However, this simple approach is able to explain the diffuse scattering of multilayers in the vicinity of the superlattice Bragg reflections which is, although measured at large angles, relatively intense.[1,2,4,8,10,12] If the angles α_i and α_f are small, dynamical effects have to be considered. In this paper dynamical effects are taken into account by using the distorted-wave Born approximation (DWBA). The formulation for the case of a rough surface within the concept of the DWBA was given by Sinha *et al.*[32] and later confirmed by Pynn.[33] The extension to multilayers was given by Holý *et al.*[34,35] who included the effects of vertical correlations.

Whereas the scattering theory within the DWBA has been worked out in great detail within recent years, only a few papers with experimental tests of these calculations have been published up to now.[35–37] The purpose of the present paper is to test the application of the theoretical results for the analysis of the diffusely scattered intensity from a special sample of technical interest where the effect of vertical correlations plays an important role. This sample is grown by molecular-beam epitaxy (MBE) and therefore small roughness of the buried interfaces are expected. We focus on the question to what extent the above restriction limits the determination of the roughness parameters.

This paper is organized as follows. In Secs. II A and II B the scattering theory of the specularly reflected and diffuse intensity, respectively, is briefly sketched. The particular model to describe the interface morphology is given in Sec. II C. The sample preparation is described in Sec. III. Then the experimental setup and the scattering geometry follow in Sec. IV. The special data analysis procedure, the measure-

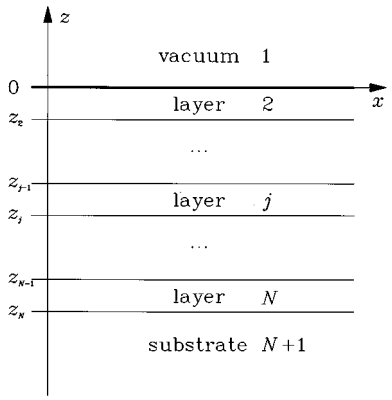

FIG. 1. Notation for a system of $N-1$ layers and N interfaces following Holý *et al.* (Ref. 34). The vacuum and the substrate are denoted by 1 and $N+1$, respectively. The x axis is in the surface plane. The z axis is parallel to the surface normal and $z_1=0$ marks the average height of the sample surface.

ments, and the discussion of the fit results are given in Sec. V, followed by a summary, conclusions, and an outlook in Sec. VI.

II. THEORY

A. Specular reflectivity

The following coordinate system is chosen in this paper. The z axis is parallel to the normal of the average surface of the sample. Its origin $z_1=0$ marks the average surface position, z_j denotes the position of the interface j, and $\mathbf{r}=(x,y)^T$ is a vector in the surface plane. The y axis is perpendicular to the scattering plane and the x axis is defined by the intersection of the scattering plane and the sample surface. Following the notation of Holý *et al.*,[34] we consider a system of $N-1$ layers ($j=2,\ldots,N$, vacuum $j=1$, substrate $j=N+1$; see Fig. 1). Each layer j is characterized by the thickness $d_j=z_{j-1}-z_j$, refractive index $n_j=1-\delta_j+i\beta_j$ (with the dispersion δ_j and the absorption β_j) and the rms roughnesses of the adjacent interfaces σ_{j-1} and σ_j. The optical constants δ_j and β_j are proportional to the electron density of layer j.

Taking into account the boundary conditions for the tangential components of the electric and magnetic fields, the ratio X_j of the amplitudes R_j and T_j of the reflected and transmitted x-ray waves within layer j can be calculated based on the formalism of Parrat[26] (see also Born and Wolf[27]):

$$X_j=\frac{R_j}{T_j}=e^{-2ik_{z,j}z_j}\frac{r_{j,j+1}+X_{j+1}e^{2ik_{z,j+1}z_j}}{1+r_{j,j+1}X_{j+1}e^{2ik_{z,j+1}z_j}}. \qquad (1)$$

The wave-vector component perpendicular to the average layer surface inside the respective medium is given by $k_{z,j}=k_1\{n_j^2-(\cos\alpha_i)^2\}^{1/2}$ with $k_1=2\pi/\lambda$ the modulus of the wave vector in the vacuum (x-ray wavelength λ) and the incidence angle α_i. The roughness is taken into account by assuming a tanh refractive index profile for the interface between the layers j and $j+1$,

$$n(z)=\frac{n_j+n_{j+1}}{2}-\frac{n_j-n_{j+1}}{2}\tanh\left[\frac{z-z_j}{\sigma_j}\left(\frac{2}{\pi}\right)^{1/2}\right]. \qquad (2)$$

Then the Helmholtz equation can be solved analytically for this particular profile yielding the Fresnel coefficients $\tilde{r}_{j,j+1}$ of a rough interface. The $r_{j,j+1}$ of a smooth interface must be replaced in Eq. (1) by[30,31,38,39]

$$\tilde{r}_{j,j+1}=\frac{\sinh[(\pi/2)^{1.5}\sigma_j(k_{z,j}-k_{z,j+1})]}{\sinh[(\pi/2)^{1.5}\sigma_j(k_{z,j}+k_{z,j+1})]}. \qquad (3)$$

Equation (3) is valid for small roughnesses ($\sigma_j<25$ Å). The tanh profile for the refractive index given by Eq. (2) is very similar to an error-function profile[36] (Gaussian probability density function), which will be assumed for the calculation of the diffuse scattering in the next section. The specularly reflected intensity I can be obtained with Eq. (1) via $I=|R_1|^2$, if the amplitude of the impinging x-ray wave is set to $T_1=1$ and a semi-infinite substrate is assumed ($R_{N+1}=0$).

B. Diffuse scattering

Detailed information about the morphology of the interfaces, i.e., the height-height autocorrelation functions and the corresponding cross-correlation functions, is obtained by analysis of the diffuse scattering. The analysis of diffuse scattering performed in this paper is based on the DWBA.

As can be seen in textbooks of quantum mechanics,[40] the DWBA is a time-dependent first-order perturbation theory. In order to determine the differential cross section of the scattered radiation, the corresponding transition matrix element must be calculated (Fermi's golden rule). The major approximation of the DWBA is the replacement of the exact solution by that of the undisturbed system within the expression for this matrix element. Sinha *et al.*[32] applied the formulation of the DWBA to the calculation of the diffuse scattering from a rough surface. The roughness is assumed to be a small perturbation of a homogeneous medium with a flat surface. The eigenstates for the calculation of the transition matrix element are given by the Fresnel formulas (see Sec. II A). Assuming a Gaussian probability density function of the surface heights, a complete statistical description of the surface can be given by the average surface position and the height-height autocorrelation function $C(\mathbf{R})$ with $\mathbf{R}=\mathbf{r}'-\mathbf{r}=(X,Y)^T$ a spatial vector in the surface plane. Recently, Holý *et al.*[34] extended this approach to layer systems. A detailed description of the calculations is given in Ref. 34 for uncorrelated interfaces and in Ref. 35 for partially and fully correlated interfaces. In the case of a system of several interfaces, a two-dimensional Gaussian probability density function of the surface heights is assumed and additional statistical information is given by the cross-correlation functions $C_{jk}(\mathbf{R})$ (for all interfaces j and k).

The calculation of the transition matrix elements within the DWBA finally leads to the expression for the cross section of the diffuse scattering:

TABLE I. Two possible analytic continuations of the fields and their respective momentum transfers [see Eqs. (4) and (5)]. $\mathbf{k}_{i;j}$ and $\mathbf{k}_{f;j}$ denote the wave vector in the medium j for the angle of incidence α_i and the exit angle α_f, respectively. The amplitudes of the transmitted and reflected electromagnetic waves are $T_{i;j}, T_{f;j}$ and $R_{i;j}, R_{f;j}$.

I		II	
$G_j^0 = T_{i;j+1} T_{f;j+1}$	$\mathbf{q}_j^0 = \mathbf{k}_{i;j+1} + \mathbf{k}_{f;j+1}$	$G_j^0 = T_{i;j} T_{f;j}$	$\mathbf{q}_j^0 = \mathbf{k}_{i;j} + \mathbf{k}_{f;j}$
$G_j^1 = T_{i;j+1} R_{f;j+1}$	$\mathbf{q}_j^1 = \mathbf{k}_{i;j+1} - \mathbf{k}_{f;j+1}$	$G_j^1 = T_{i;j} R_{f;j}$	$\mathbf{q}_j^1 = \mathbf{k}_{i;j} - \mathbf{k}_{f;j}$
$G_j^2 = R_{i;j+1} T_{f;j+1}$	$\mathbf{q}_j^2 = -\mathbf{q}_j^1$	$G_j^2 = R_{i;j} T_{f;j}$	$\mathbf{q}_j^2 = -\mathbf{q}_j^1$
$G_j^3 = R_{i;j+1} R_{f;j+1}$	$\mathbf{q}_j^3 = -\mathbf{q}_j^0$	$G_j^3 = R_{i;j} R_{f;j}$	$\mathbf{q}_j^3 = -\mathbf{q}_j^0$

$$\left(\frac{d\sigma}{d\Omega}\right)_{\text{diff}} = \frac{\mathcal{G} k_1^2}{8\pi^2} \sum_{j,k=1}^{N} (n_j^2 - n_{j+1}^2)(n_k^2 - n_{k+1}^2)^* \times \sum_{m,n=0}^{3} \tilde{G}_j^m \tilde{G}_k^{m*} \exp\{-\tfrac{1}{2}[(q_{z,j}^m \sigma_j)^2 + (q_{z,k}^{n*} \sigma_k)^2]\} \mathcal{S}_{jk}^{mn}(q_x) \tag{4}$$

with the structure factor

$$\mathcal{S}_{jk}^{mn}(q_x) = \frac{1}{q_{z,j}^m q_{z,k}^{n*}} \int_0^\infty dX [\exp\{q_{z,j}^m q_{z,k}^{n*} C_{jk}(X)\} - 1] \times \cos(q_x X). \tag{5}$$

Due to the rather coarse resolution perpendicular to the scattering plane, an integration over the wave-vector transfer q_y was already performed in Eq. (5). The lateral roughness structure of the interfaces in the direction x is taken into account in Eq. (5) by the autocorrelation functions $C_{jj}(X) = C_j(X)$ and the corresponding cross-correlation functions $C_{jk}(X)$. The illuminated area of the sample is denoted by $\mathcal{G}$, $\mathbf{q}_j^m = (q_x, q_{z,j}^m)^T$ is the momentum transfer within each layer, and dynamical effects are taken into account by the factors $\tilde{G}_j^m = G_j^m \exp(-i q_{z,j}^m z_j)$. The respective expressions for G_j^m and $\mathbf{q}_j^m$ are given in Table I. With the restriction to identical analytic continuations for all interfaces four different sets G_j^m are possible. But only the two realizations given in Table I fulfill the condition that the differential cross section [Eqs. (4) and (5)] has to be invariant against an exchange of the position of the x-ray source and the detector. Numerical tests for the given data set show that the difference between the diffuse intensities calculated with different analytical continuations can be neglected for our system.

For small q_z values the exponential in the integral of Eq. (5) can be replaced by the first two terms of its Taylor series. This was done in the paper of Holý *et al.*[34] Then for $j = k$ the integral equals the power spectral density $L_j(q_x)$ of the interface j. We have performed simulations which show that $|q_z \sigma| = 1$ is a realistic limit for the validity of this approximation. In our case the difference between the complete solution [Eq. (5)] and the above approximation is significant. Therefore the diffuse scattering was calculated using the full expression [Eqs. (4) and (5)].

For large angles of incidence α_i and exit angles α_f, the expressions for G_j and $q_{z,j}$ can be simplified to

$$G_j^m G_k^{m*} = \delta_{m0} \delta_{n0},$$

$$q_{z,j}^1 = -q_{z,j}^2 = k_1 \{\sin(\alpha_i) - \sin(\alpha_f)\}, \qquad q_{z,j}^0 = -q_{z,j}^3 = k_1 \{\sin(\alpha_i) + \sin(\alpha_f)\}, \tag{6}$$

and Eqs. (4) and (5) reduce to the kinematical formulation (simple BA) for multilayers given, e.g., by Phang *et al.*[2] and Sanyal *et al.*[41] Therefore Eqs. (4) and (5) are exact for $|q_z \sigma| \ll 1$ (small perturbations) as well as for large $|q_z \sigma|$ values (the kinematical limit). Furthermore, de Boer has shown for one interface[23] that the DWBA is a good approximation even in the second order of $|q_z \sigma|$. Thus we have chosen Eqs. (4) and (5) for the calculation of the diffuse scattering in the intermediate region $|q_z \sigma| \approx 1$.

C. Roughness description

In order to calculate the diffuse scattering, the correlation functions $C_{jk}(X) = \langle \phi_j(x) \phi_k(x+X) \rangle_x \quad (j,k = 1, \ldots, N)$ must be specified. $\phi_j(x)$ denotes the height of the interface j at the lateral position x with respect to the average interface z_j.

In the present work, all interfaces are assumed to have self-affine shapes,[42,43] limited by a finite lateral cutoff.[32] This approach may be justified for MBE-grown layer systems[44] and leads to autocorrelation functions

$$C_j(X) = \sigma_j^2 \exp\{-(X/\xi_j)^{2h_j}\}. \tag{7}$$

The shape of this function is defined by the cutoff length ξ_j and the Hurst parameter h_j of the interface j. The quantity ξ_j plays the role of a lateral length scale and the Hurst parameter h_j is defined by the fractal box dimension $D_j = 3 - h_j$ of the interface (note that $0 < h_j \leqslant 1$). The convenience of this model for the interface shapes of the present sample will be discussed in Sec. V C.

In order to describe the propagation of the roughness from interface j to k, the so-called replication factor $\chi_{jk}(q_x)$ (Ref. 9) is introduced:

$$\tilde{\phi}_k(q_x) = \chi_{jk}(q_x) \tilde{\phi}_j(q_x), \tag{8}$$

with

$$\tilde{\phi}_j(q_x) = |\tilde{\phi}_j(q_x)| \exp\{i \varphi_j(q_x)\} = \frac{1}{\sqrt{2\pi}} \int_{-\infty}^{\infty} dx \phi_j(x) \exp(-i q_x x). \tag{9}$$

Here $\tilde{\phi}_j(q_x)$ denotes the one-dimensional Fourier transform of the interface j with modulus $|\tilde{\phi}_j(q_x)|$ and phase $\varphi_j(q_x)$. Equation (8) describes how a particular spatial frequency

q_x of the roughness spectrum of interface j propagates through the stack to layer k.[45] Solving the continuum equation, which describes the evolution of the surface profile as a function of film thickness, yields the replication factor. This was done, e.g., for the linearized Langevin equation (Edwards-Wilkinson model[46]) by Spiller, Stearns, and Krumrey.[9] Several other growth models[15,17,18] have been established, taking into account effects like surface diffusion, desorption (evaporation), fluctuations of the flux of the incident particle beam, and the dependence of the growth velocity on the local surface orientation.

Using the definition of the replication factor $\chi_{jk}(q_x)$ [Eq. (8)] and the power spectral density $L_j(q_x)=|\tilde{\phi}_j(q_x)|^2$ one obtains

$$L_k(q_x)=|\chi_{jk}(q_x)|^2 L_j(q_x). \tag{10}$$

Then the quantity $L_{jk}(q_x):=\tilde{\phi}_j(q_x)^*\tilde{\phi}_k(q_x)$ is given by

$$L_{jk}(q_x)=\chi_{jk}(q_x)L_j(q_x). \tag{11}$$

According to the Wiener-Khinchin theorem[47] the autocorrelation function $C_j(X)$ of the interface j is given by the inverse Fourier transform of the power spectral density $L_j(q_x)$. In an analogous manner it can be shown that the inverse Fourier transform of the quantity $L_{jk}(q_x)$ yields the cross-correlation function $C_{jk}(X)$. Therefore it is possible to calculate the cross-correlation functions and all autocorrelation functions $C_k(x)$ $(k=1,\ldots,N-1)$, if the autocorrelation function of the substrate $C_N(x)$ and the replication factors $\chi_{jk}(q_x)$ for a growth model are given. This was done by Spiller *et al.* for the special case of a multilayer consisting of bilayers with constant layer thicknesses including intrinsic roughnesses. But this procedure is not convenient in the case of the complex preparation procedure of the present sample (see Sec. III). The growth parameters were changed several times even during the preparation of one layer. For every preparation step a corresponding replication factor $\chi_{jk}(q_x)$ ought to be introduced which would lead to an increasing number of fit parameters.

Therefore another approach was chosen. According to Eq. (11), the cross-correlation function $C_{jk}(X)$ of the corresponding interfaces j and k depends on the modulus as well as on the phase of the replication factor $\chi_{jk}(q_x)$. The modulus is given by the power spectral densities $L_j(q_x)$ and $L_k(q_x)$ [Eq. (10)] and therefore by the autocorrelation functions $C_j(X)$ and $C_k(X)$ of self-affine interface shapes [Eq. (7)]. The autocorrelation functions could be determined, too, if the interfaces j and k would be considered isolated from each other. On the other hand, the cross-correlation function $C_{jk}(X)$ yields a statistical description of the system consisting of *both* interfaces. Therefore $C_{jk}(X)$ additionally depends on the relationship between the phases $\varphi(q_x)$ and $\varphi_j(q_x)$ of the Fourier components of the two interfaces. According to Eq. (8), the phase difference $\varphi_k(q_x)-\varphi_j(q_x)$ equals the phase of the replication factor $\chi_{jk}(q_x)$. After assuming a q_x-independent Gaussian distribution of the phase of the replication factor with dimensionless width $\sigma_{\varphi,jk}$ and mean value zero and subsequently performing the ensemble average, Eq. (11) leads to

$$L_{jk}(q_x)=\{L_j(q_x)L_k(q_x)\}^{1/2}\exp(-|z_j-z_k|/\xi_\perp). \tag{12}$$

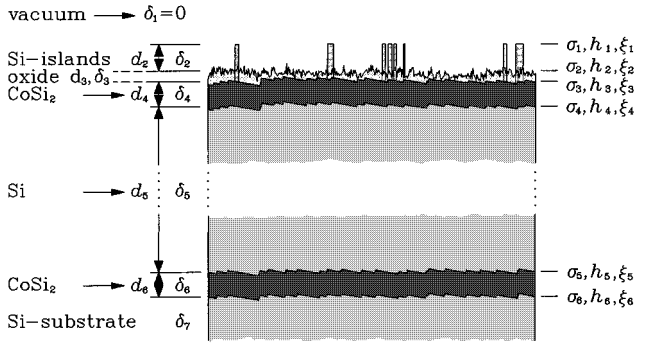

FIG. 2. Cross section of the investigated sample showing a lateral region of 4 μm. The perpendicular length scale is magnified by a factor of 10 with respect to the lateral scale. The shade roughly reflects the density of the corresponding layer. The symbols describe the averaged perpendicular structure (left side) of the sample as well as the lateral roughness shape (right side) and correspond to the notation given in Fig. 1. The interface shapes 2–6 are simulations according to the parameters determined by the x-ray investigation as discussed in Sec. V C.

The vertical correlation length $\xi_\perp$, which has already been introduced by Sanyal *et al.*,[41,48] is defined in this paper by $\xi_\perp=2|z_j-z_k|/\sigma^2_{\varphi,jk}$. In order to reduce the number of free parameters it is assumed, that $\xi_\perp$ is independent of j and k.

The calculations of the cross-correlation functions $C_{jk}(X)=C_{jk}(X,0)$ presented in this section has been performed only in one-dimension [see Eqs. (8)–(12)]. In principle a two-dimensional treatment is required and Eq. (12) has to be replaced by

$$L_{jk}(\mathbf{q}_\parallel)=\{L_j(\mathbf{q}_\parallel)L_k(\mathbf{q}_\parallel)\}^{1/2}\exp(-|z_j-z_k|/\xi_\perp) \tag{13}$$

with $\mathbf{q}_\parallel=(q_x,q_y)^T$. But the two-dimensional calculation of the cross-correlation functions is rather complex for the following two reasons. (i) The numerical calculation is very time consuming even for the one-dimensional approach (see Sec. V A) and would be further increased by the use of two-dimensional Fourier transforms. (ii) A two-dimensional model for the interface roughness, i.e., $C_{jk}(X,Y)$, is needed and leads to additional fit parameters. In order to avoid these shortcomings, we restrict ourselves to the one-dimensional treatment of the cross-correlation functions within the fit procedure. Subsequently, for the resulting set of parameters the complete calculation of the cross-correlation functions has been performed in two dimensions. Fortunately it turns out that the difference between our simplified one-dimensional treatment and the two-dimensional calculations is negligible (see the discussion in Sec. V C).

III. SAMPLE

A schematic cross section of the investigated MBE-sample is shown in Fig. 2. The symbols characterize the perpendicular structure of the sample as well as the lateral roughness shape and correspond to the notation given in Fig. 1. The distances of the interfaces and their shapes are explained in Sec. V C. The sample consists of two thin ($\approx$30 Å) $CoSi_2$ layers separated by a Si layer with a thickness of $\approx$500 Å. An n-doped Si(111) wafer with a miscut of 0.17° overgrown by a Si buffer layer was used as substrate, which

TABLE II. Results of the simultaneous fits of the x-ray measurements compared with those of various other experimental techniques. In order to estimate the errors of the x-ray measurements, the parameters were varied, starting with the fit results, until a significant increase of the difference between the data and the calculation was observable. Errors of the STM analysis stem from the finite size of the micrograph.

Probe		X-ray simultan. fitted	RBS	TEM	Quartz thickness monitor	STM
Oxide	σ_3 (Å)	0.9 ± 0.3				2.0 ± 0.5
	h_3	0.24 ± 0.10				0.45 ± 0.10
	ξ_3 (Å)	2200 ± 500				1800 ± 200
$CoSi_2$	d_4 (Å)	31.6 ± 0.4	30.4–31.3		31	
Si	d_5 (Å)	494.0 ± 0.4	500	500	500	
$CoSi_2$	d_6 (Å)	33.4 ± 0.5	28.4–30.7	34	25	
Miscut μ		$0.171°\pm0.005°$				$0.21°\pm0.1°$

exhibits a clean, 7×7 reconstructed surface observed by reflection high-energy electron diffraction (RHEED) before buffer growth. The $CoSi_2$ layers are prepared by the so-called *template* technique,[49] which is described in detail by v. Känel in Ref. 50. The Si layer is grown as a series of evaporation steps and interruptions due to annealing procedures. The nominal layer thicknesses listed in Table II were determined by the frequency shift of a quartz thickness monitor. The deposition of Si on top of the upper $CoSi_2$ layer is a widely used method to stabilize the surface. For this sample, the amount of Si was somewhat too high and this results in an island formation. The scanning tunneling microscopy (STM) micrograph (Fig. 3) reveals Si islands with diameters of approximately 500–1000 Å and average heights of ≈35 Å, which cover $\approx5\%$ of the surface of the sample.

There are several reasons for choosing this sample as a model system for the analysis of the diffuse scattering of rough surfaces. (i) Thin buried $CoSi_2$ layers with flat interfaces are playing an important role in microelectronic applications as metallic layers of high conductivity or, e.g., as gate electrodes in permeable base transistors. High-quality $Si/CoSi_2$ heterostructures may eventually lead to the development of stacked devices, i.e., three-dimensional integration.[50] (ii) The STM micrograph of the sample surface shows a regular monolayer step structure similar to that observed for the substrate surface produced by the misorientation of the delivered Si wafer (see Fig. 3). This fact and the regular, epitaxial growth of these MBE samples support the assumption that conformal roughness dominates the interface structures. In contrast to this, it has turned out that $CoSi_2$ layers prepared with the ion-beam-synthesis (IBS) technique show uncorrelated interfaces.[51,52] Therefore, IBS samples are not appropriate for a detailed investigation of diffuse scattering within the DWBA including vertical correlations. (iii) Another point is that the large contrast of the electron density between Si and $CoSi_2$ is favorable for x-ray-scattering experiments.

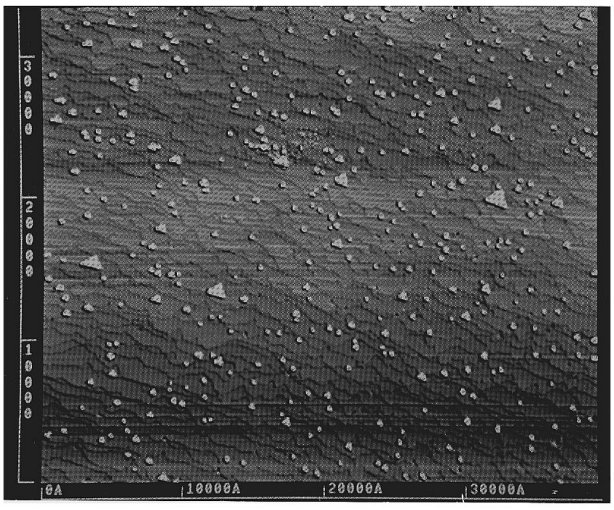

FIG. 3. STM micrograph of the surface of the upper $CoSi_2$ layer, performed just after the preparation of the sample. The Si islands and the step structure can clearly be seen.

IV. EXPERIMENTAL SETUP AND SCATTERING GEOMETRY

A. Setup

Most of the measurements were performed on a two-crystal diffractometer using an 18 kW rotating-anode generator (Siemens XP18) with a copper target as x-ray source. The Ge(111) monochromator in combination with a slit selects the Cu $K\alpha_1$ radiation (wavelength $\lambda=1.540\,56$ Å). A slit of dimension 10×1 mm^2 in front of the sample and a pair of slits (10×0.2 mm^2) 200 and 800 mm behind the sample define the angle of incidence α_i and the exit angle α_f, respectively. The sample surface is oriented perpendicular to the scattering plane. The resolution of the instrument within the scattering plane in the region of total external reflection is given by $\delta q_z\approx0.006$ Å^{-1} for the direction perpendicular and $\delta q_x\approx2\times10^{-4}\times q_z$ parallel to the surface. In addition, measurements at high q_z values were carried out using synchrotron radiation from the storage ring DORIS III on the wiggler beamline (station ROEWI) at HASYLAB, Hamburg. The wavelength for these experiments was $\lambda=1.659$ Å. This is just above the Co absorption edge and was chosen to reduce the absorption of the $CoSi_2$ layers. A detailed description of the diffractometer is given by Feidenhans'l.[53] The resolution of this diffractometer was $\delta q_z\approx0.006$ Å^{-1} and $\delta q_x\approx3\times10^{-4}\times q_z$. For both diffractometers the resolution

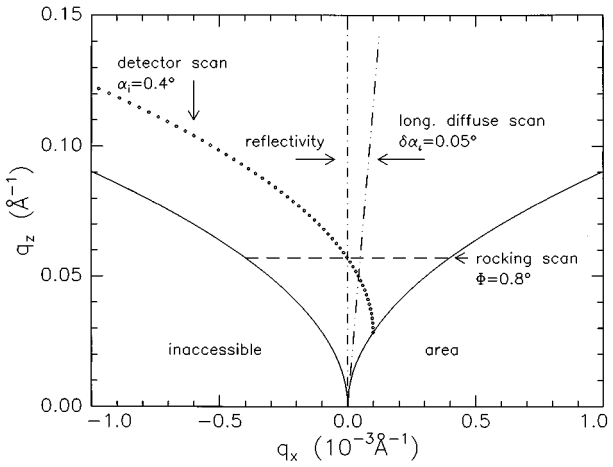

FIG. 4. Scans in reciprocal space (q_x, q_z). The dash-dotted $(\cdot\text{—}\cdot\text{—}\cdot)$ line is the path of specular reflectivity. A rocking scan with scattering angle $\Phi=\alpha_i+\alpha_f$ is marked by the dashed (— — —) line and the dashed-double-dotted $(\cdot\cdot\text{—}\cdot\cdot\text{—}\cdot\cdot\text{—})$ line is a longitudinal diffuse scan with an offset $\delta\alpha_i=0.05°$. The path of a detector scan for an angle of incidence $\alpha_i=0.4°$ is given by the dotted line $(\cdot\ \cdot\ \cdot)$. The region below the solid line is not accessible with the setup used in this work.

perpendicular to the scattering plane δq_y is rather coarse. This leads to an effective integration over q_y which was already done in Eq. (5).

B. Scattering geometry

The scans which were performed are representative cuts throughout reciprocal space. In order to illustrate the four different types of scans, their paths are shown in Fig. 4. The momentum transfer in and perpendicular to the surface plane is given by $q_x=k_1(\cos\alpha_f-\cos\alpha_i)\approx k_1\Phi/2(\alpha_i-\alpha_f)$ and $q_z=k_1(\sin\alpha_i+\sin\alpha_f)\approx k_1\Phi$, respectively. The scattering angle is denoted by $\Phi=\alpha_i+\alpha_f$. The reflectivity $(\alpha_i=\alpha_f)$ is a scan along the q_z axis $(q_x=0)$. If the angle of incidence α_i is slightly out of the specular condition $(\alpha_i=\Phi/2+\delta\alpha_i)$, a so-called longitudinal diffuse scan with offset $\delta\alpha_i$ is performed. The path of this scan in (q_x, q_z) space is a straight line slightly inclined with respect to the q_z axis. If the sample is rotated ($\Phi=$const), a rocking scan is performed. Thus, rocking scans are nearly q_x scans with $q_z\approx$const and they are also denoted as transverse scans. A detector scan is performed by varying the scattering angle Φ without changing the angle of incidence α_i. This scan follows a parabola in reciprocal space.

V. MEASUREMENTS AND DISCUSSION

A. Data analysis

To obtain the interface parameters the specular and the off-specular scans which were performed have to be fitted by the aforementioned model. It turns out that a simultaneous data analysis is necessary. This means that all scans are treated as only one data set. It should be noted that then the reflectivity is only one curve in a set of 18 scans. The advantage of this procedure is that one consistent set of model parameters is obtained, which explains both the diffuse as well as the true specular measurements. The amount of diffuse intensity in the specular direction $(\alpha_i=\alpha_f)$ is automatically calculated with the same parameters which were used for the fits of the diffuse scans. The specular reflectivity then is calculated by adding up the *true* specular (see Sec. II A) and the underlying diffuse scattering [Eqs. (4) and (5) in Sec. II B].

A method widely used to extract the true specular intensity is the subtraction of a longitudinal diffuse scan. The offset $\delta\alpha_i$ is chosen as small as possible, yet still eliminating the influence of the specular peak. Afterwards the true specular intensity is analyzed by the formulas given in Sec. II A and yields the average electron density profile of the sample. The diffusely scattered intensity (i.e., all other scans) is then calculated by using these fixed parameters. This method was successful for many systems but fails if the diffuse intensity sharply peaks under the specular peak. Numerical tests show that this is the case if the correlation length ξ_j is large and the Hurst parameter h_j becomes small.[32,33]

In this paper both procedures, the separate analysis of the true specular reflectivity as well as a simultaneous analysis of the whole data set, have been carried out. The comparison of the corresponding fit results reveals agreement for many parameters but also notable differences. A detailed discussion of this important point is given in Sec. V C.

Two additional parameters have been introduced which take into account (i) the intensity of the primary beam which determines the absolute intensity, and (ii) the ratio of the diffuse and the true specular scattering. The second parameter is directly obtained from the measurement and is *not* a free fit parameter. Geometrical effects are considered by taking into account both the illuminated area of the $CoSi_2$ surface defined by the slit in front of the sample and the α_f-dependent part of the scattered intensity which passes the two slits positioned between the sample and the detector.[54] The specularly reflected beam was fitted assuming a Lorentzian line shape for the measurements carried out at the laboratory source,[54] whereas it turns out that for the data set obtained at the synchrotron a Gaussian line shape has to be chosen. Finally, the calculated intensities were convoluted with the known resolution of the respective diffractometer.

The numerical work has been performed on a SUN4/80(SPARC10) workstation. Restricting conformal roughness to the lower interfaces (3–6; see Fig. 3) and with the parameter set of Table III typical CPU times are about 250 s for one iteration of the fit program.

B. Measurements

We have measured the reflectivity, one longitudinal diffuse scan with offset $\delta\alpha_i=0.1°$, four transverse scans at q_z values $q_z<0.089$ Å^{-1}, and five detector scans for different incident angles $\alpha_i\leqslant 0.785°$ using the laboratory source ($\lambda=1.540\,56$ Å). Furthermore, at the synchrotron with a wavelength $\lambda=1.6591$ Å a second reflectivity as well as a longitudinal diffuse scan ($\delta\alpha_i=0.05°$) were carried out and the data set was completed by five transverse scans for rather high values of q_z ($0.100<q_z<0.659$ Å^{-1}). All these scans together are the data set which is compared to the theory.

Because of the stepped interfaces, a slight dependence of the diffuse scattering on the angle γ between the x axis and

TABLE III. Results of the simultaneous fits of the specular reflectivity and the diffuse scattering measurements (second column) and the separate fit of the *true* specular reflectivity after the subtraction of a longitudinal diffuse scan (third column). The interface parameters σ_j, h_j, and ξ_j characterize the lower interface of the respective layer j (see Fig. 1). The optical constants δ for the evaporated layers and the substrate are set to the theoretical bulk values (in parentheses) for the wavelength $\lambda = 1.540\,56$ Å (laboratory source). In order to estimate the errors, the parameters were varied, starting with the fit results, until a significant increase of the difference between the data and the calculation was observable.

		All scans simultan. fitted	True specular separately fitted
Vacuum	σ_1 (Å)	34.3±4.0	
	h_1	0.14±0.10	
	ξ_1 (Å)	27 000±4 000	
S islands	d_2 (Å)	34.4±5.0	
	$\delta_2\times10^6$	3.0±0.5	
	σ_2 (Å)	4.4±0.5	8.7±0.1
	h_2	0.12±0.10	
	ξ_2 (Å)	800±500	
Oxide	d_3 (Å)	11.2±1.0	9.0±0.5
	$\delta_3\times10^6$	6.5±0.6	7.8±0.6
	σ_3 (Å)	0.9±0.3	<0.5
	$h_3=h_4$	0.24±0.10	
	$\xi_3=\xi_4$ (Å)	2200±550	
$CoSi_2$	d_4 (Å)	31.6±0.4	32.2±0.4
	$\delta_4\times10^6$	(14.7)	(14.7)
	σ_4 (Å)	1.4±0.4	1.2±0.3
	$h_4=h_3$	0.24±0.10	
	$\xi_4=\xi_3$ (Å)	2200±500	
Si	d_5 (Å)	494.0±0.4	494.3±0.4
	$\delta_5\times10^6$	(7.56)	(7.56)
	σ_5 (Å)	<0.5	1.0±0.3
	$h_5=h_6$	0.65±0.2	
	$\xi_5=\xi_6$ (Å)	600±300	
$CoSi_2$	d_6 (Å)	33.4±0.5	33.7±0.3
	$\delta_6\times10^6$	(14.7)	(14.7)
	σ_6 (Å)	0.9±0.4	1.2±0.2
	$h_6=h_5$	0.65±0.2	
	$\xi_6=\xi_5$ (Å)	600±300	
Si substrate	$\delta_7\times10^6$	(7.56)	(7.56)
	$\xi_\perp$ (Å)	450±200	
Miscut μ		0.171°±0.005°	

the steps (i.e., the orientation of the sample with respect to the primary beam) has been found for transverse scans at $q_z = 0.264$ Å^{-1}. Although a systematic investigation of the anisotropy of the diffuse scattering within the region of total external reflection has not been performed within this work,[55] the angle γ as well as the miscut μ must be determined. Therefore transverse scans for $q_z = 1.054$ Å^{-1} were performed. Due to the high quality of the interfaces, the reflectivity peak and the crystal truncation rod[56,57] (CTR) of the symmetrical 111 Bragg reflection with wave-vector transfer $\mathbf{Q}_{111}$ are present in those transverse scans for $q_z = 1.054$ Å$^{-1} \approx |\mathbf{Q}_{111}|/2$. The two peaks occur at the same angle of incidence $\alpha_i = \alpha_i^{\mathrm{refl}} = \alpha_i^{\mathrm{CTR}}$, if the steps are parallel to the x axis (i.e., $\gamma = 0°$). Then the sample was rotated 90° around the surface normal. The x axis is now perpendicular to the steps ($\gamma = 90°$) and the angle between the vector $\mathbf{Q}_{111}$ and the q_z axis equals the miscut μ of the sample (see Fig. 5). The difference of the peak positions $\alpha_i^{\mathrm{refl}} - \alpha_i^{\mathrm{CTR}}$ is directly related to the miscut of the sample: $\mu \approx |\alpha_i^{\mathrm{refl}} - \alpha_i^{\mathrm{CTR}}| q_z / |\mathbf{Q}_{111}|$. This miscut determination involves only short motor movements of the diffractometer and therefore small instrumental uncertainties. It was found that for the measurements presented in this paper the orientation of the sample was $\gamma = 30° \pm 5°$.[58] The miscut of the substrate is determined to $\mu = 0.171° \pm 0.005°$.

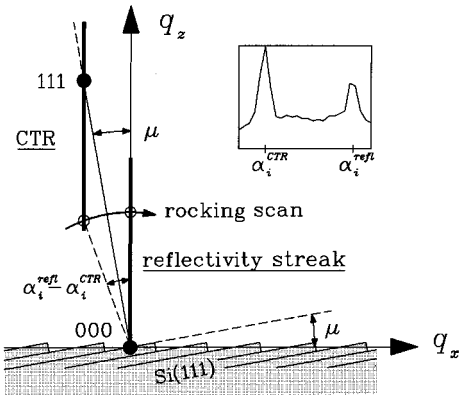

FIG. 5. Principle sketch of the miscut determination for a vicinal Si(111) surface. The q_z axis is parallel to the average surface normal. The miscut μ of the sample is defined as the angle between the surface and the Si(111) lattice planes, if $\gamma = 90°$ (i.e., the x axis is in the average surface plane and perpendicular to the steps). The angle μ can be found again between the q_z axis and the wave-vector transfer $\mathbf{Q}_{111}$ of the symmetrical 111 Bragg reflection. The inset shows a rocking scan for $q_z \approx |\mathbf{Q}_{111}|/2$ which crosses the CTR of the 111 reflection and the reflectivity streak. The difference of the peak positions $\alpha_i^{\mathrm{refl}} - \alpha_i^{\mathrm{CTR}}$ is directly related to the miscut μ of the sample (see text).

The upper curves in Fig. 6 represent the measurement (crosses) and the fit from the simultaneous analysis (solid line) of the specular reflectivity for the wavelength $\lambda = 1.6591$ Å (ROEWI). The inset shows an enlargement of the curves within the region $0.05 \leq q_z \leq 0.12$ Å^{-1} and the numbers (1–9) mark the q_z positions where transverse scans were taken. The reflectivity is mainly sensitive to the average electron density profile in the z direction (see Sec. II A). The short-period oscillations stem from the interference of the x rays scattered at the interfaces of different $CoSi_2$ layers. Additionally, a beating can be seen which is related to the small thicknesses of the $CoSi_2$ layers (≈ 30 Å). Due to the weak damping of the oscillations one can conclude that the interfaces of the epitaxial layers are extremely smooth. For comparison, in Fig. 6 the best fit (solid line, lower curve) of the separately analyzed *true* specular reflectivity (crosses, lower curve) is given. The difference of the results and the quality of the fits for the two methods of data analysis will be discussed in Sec. V C. As already mentioned, the high quality of the interfaces allows a measurement of the reflectivity within a large region $0 \leq q_z \leq 0.8$ Å$^{-1} = 0.4|\mathbf{Q}_{111}|$. Nevertheless, a perturbation of the reflectivity by the crystal structure of the sample (i.e., the CTR of the 111 Bragg reflection) can be

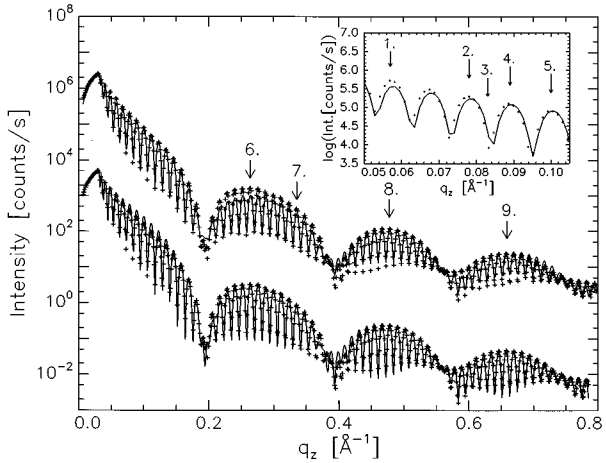

FIG. 6. The specular reflectivity (upper curve, crosses) and the *true* specular part (lower curve, crosses) together with the best fits (solid lines). The measurement has been performed at the synchrotron ($\lambda = 1.6591$ Å). The different analysis procedures for both data sets are explained in the text. The numbers (1–9) mark the positions where the transverse scans which are shown in Figs. 7 and 8 were performed. The curves have been shifted for clarity. The inset shows an enlargement of the upper curves within the region $0.05 \leq q_z \leq 0.12$ Å^{-1}.

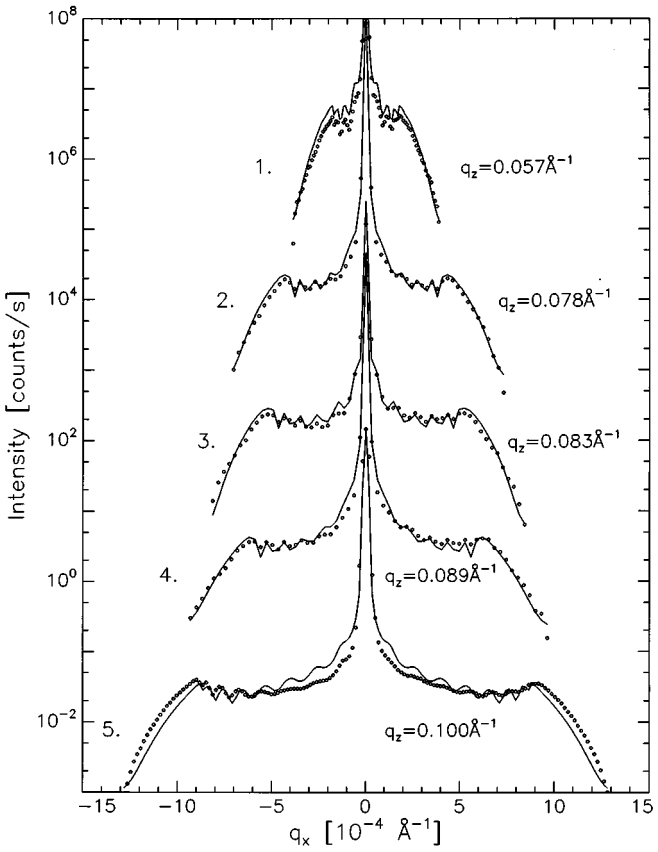

FIG. 7. Rocking scans performed for different q_z values in the region $0.057 \leq q_z \leq 0.100$ Å^{-1}. The scans denoted by 1–4 have been carried out at the laboratory source ($\lambda = 1.540\,56$ Å) and curve 5 is obtained by using synchrotron radiation ($\lambda = 1.6591$ Å). The solid lines denote the best fit and the open symbols are the measurements. The curves have been shifted for clarity.

definitely excluded because of the miscut of the sample. Therefore the specular ridge is clearly separated from the CTR (see Fig. 5).

In Figs. 7 and 8 the series of transverse scans at q_z values $0.057 < q_z < 0.100$ Å^{-1} and $0.264 < q_z < 0.659$ Å^{-1} are presented. Open symbols are the measurements and the fits are given by solid lines. The so-called Yoneda peaks,[59] which occur if either α_i or α_f equals the critical angle of total external reflection, and the thickness oscillations[35] between the Yoneda peaks stem from dynamical scattering processes at the interfaces. As can be seen in Fig. 7, only the Yoneda wing corresponding to the critical angle of Si $\alpha_{c,\mathrm{Si}} = 0.22°$ (for $\lambda = 1.540\,56$ Å) is visible. The minimum value of the scattering depth[60] $\Lambda = 23$ Å for $CoSi_2$ is close to the thicknesses (≈ 30 Å) of the thin $CoSi_2$ layers. For superlattice structures, instead of modulations the diffuse scattering exhibits sharp peaks, which are also called Bragg-like peaks.[35] With increasing q_z values, the influence of dynamical effects on the transverse scans decreases, which is clearly shown by the small intensity of the Yoneda peaks for the transverse scans 8 and 9. Additionally, the range of spatial roughness frequencies covered by the experiment increases. Therefore, the rocking curves presented in Fig. 8 are more sensitive to the detailed structure of the interface shapes. Unfortunately, these scans are slightly asymmetric. Additional diffuse intensity on the left side ($q_x < 0$ Å^{-1}) of these transverse scans stems from a small area of the surface which is not as well grown as the rest of the surface. In order to determine the influence of this surface area on the diffuse intensity in more detail, transverse scans at low q_x values have been performed with different vertical slit settings. The comparison of the respective shapes of the rocking scans shows that the influence is limited to the region $q_x < 0$ Å^{-1}. Therefore the measurements shown in Fig. 8 were analyzed correctly for $q_x > 0$ Å^{-1}.

Figure 9 shows the detector scans carried out for five different angles of incidence α_i (measurements open symbols, fits solid lines). Short-period ($\Delta\alpha_f^{\mathrm{dyn}}$) oscillations due to dynamical scattering at the interfaces of the sandwiched Si layer are limited to a region between the Yoneda wing and the specular peak. For $\alpha_f > \alpha_i$, oscillations with period $\Delta\alpha_f^{\mathrm{conf}} = 2\Delta\alpha_f^{\mathrm{dyn}}$ occur. According to Ref. 35, the simulations shown in Fig. 10 demonstrate that these long-period oscillations are caused by conformal roughness. The perpendicular correlation length $\xi_\perp$ is at least in the range of the sandwiched Si layer thickness ($d_{\mathrm{Si}} \approx 500$ Å). Thus interfaces of different $CoSi_2$ layers are partially correlated. For the simulations presented in Fig. 10 as well as for the fit, only correlations between interfaces of the evaporated layers have been assumed. The inclusion of conformal roughness connected with the upper interfaces indicated in Fig. 2 as 1 and 2 (see Sec. V C) does not improve the fits significantly.

The longitudinal diffuse scans carried out for offset angles $\delta\alpha_i = 0.05°$ and $0.1°$ are presented in Fig. 11. The long-period oscillations stem from the highly correlated interfaces of the *same* $CoSi_2$ layer. Furthermore, the measurement exhibits weak rapid oscillations. Calculations performed for different values of the perpendicular correlation length $\xi_\perp$ (see Fig. 12) show that these rapid oscillations are *no* hint for conformal roughness, if they are limited to the vicinity of the

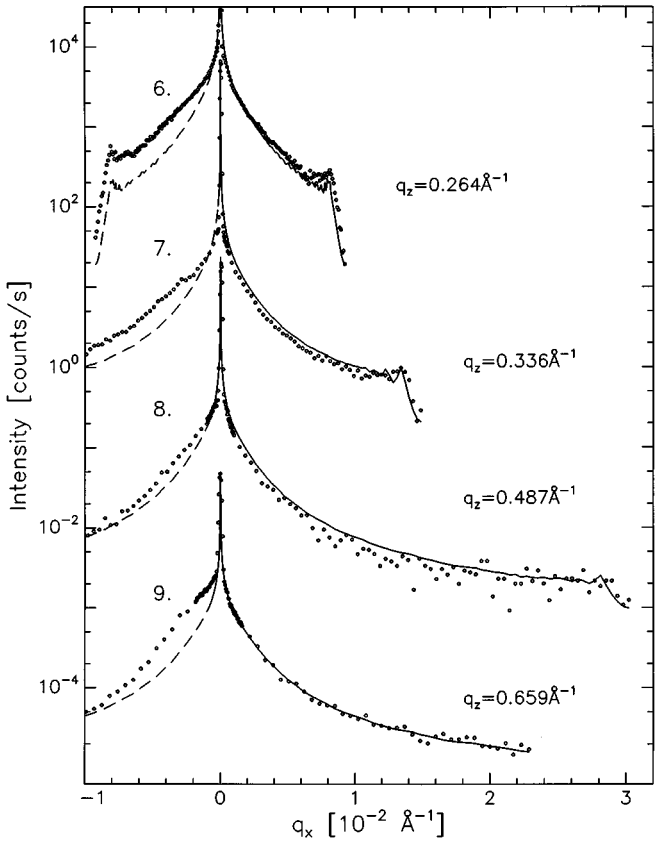

FIG. 8. Rocking scans performed for different q_z values in the region $0.264 \leq q_z \leq 0.659$ Å^{-1}. The measurements have been performed at the synchrotron ($\lambda = 1.6591$ Å) and are denoted by open symbols. Note that the fits have been carried out only for the region $q_x > 0$ Å^{-1} (solid line, see text). The curves have been shifted for clarity.

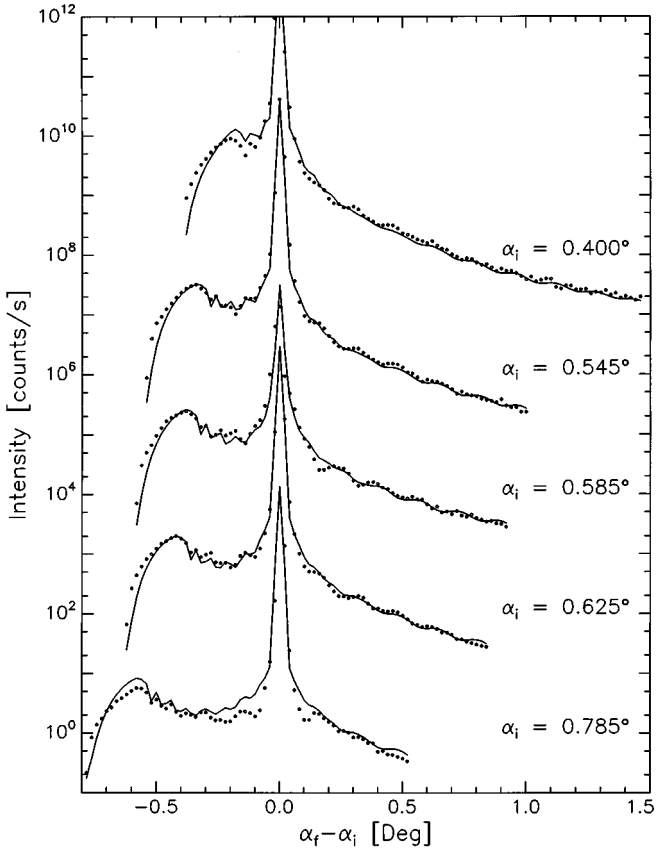

FIG. 9. Detector scans for different angles of incidence α_i, performed at the laboratory source ($\lambda = 1.540\,56$ Å). The solid lines denote the best fit and the open symbols are the measurements. The curves have been shifted for clarity.

Yoneda peak. However, if they also occur for large values of q_z conformal roughness has to be assumed. The small magnitude of the oscillations measured for large q_z (see the insets of Figs. 11 and 12) leads to the conclusion that the perpendicular correlation length does not exceed $\xi_\perp \approx 650$ Å.

The simulations shown in Figs. 10 and 12 reveal that for the present sample the detector scans are more sensitive to the perpendicular correlation length than the longitudinal diffuse scans. Mainly the short-period modulations in both scan types determine the value of the perpendicular correlation length $\xi_\perp$, because $\xi_\perp$ is in the range of the interface distance of different $CoSi_2$ layers (≈ 500 Å) and much larger than the thicknesses of the $CoSi_2$ layers. These rapid oscillations due to conformal roughness are better visible in the detector scans: the intensity of the longitudinal diffuse scans quickly decreases with increasing q_z. Furthermore, the region $0 < q_z \leq 0.1$ Å^{-1} is strongly influenced by oscillations stemming from dynamical effects (see Fig. 12, curve for $\xi_\perp = 0$ Å). In contrast to detector scans, in longitudinal diffuse scans the period of the oscillations due to dynamical effects and conformal roughness, respectively, is identical,[35] which makes the separation of the two effects difficult.

C. Discussion

Results of the least-squares fits performed on the whole set of x-ray measurements are presented in the second column of Table III. The third column of Table III contains the results of the separate analysis of the *true* specular reflectivity. For comparison, the thicknesses of the evaporated layers (d_4, d_5, d_6) determined by Rutherford backscattering/channeling (RBS) and quartz thickness monitor measurements as well as transmission electron microscopy (TEM) micrographs are listed in Table II. Furthermore, the analysis of the STM micrograph (Fig. 3) reveals the lateral roughness structure of the sample surface (just after the preparation, still under UHV conditions; interface 3 in Fig. 2). The results are given in the last column of Table II.

The statistical analysis of the STM micrograph has been carried out as follows. The whole picture of 3.5×3.5 μm^2 was analyzed. Approximately 25 monolayer step positions on 46 straight lines parallel to the direction of the cut of the surface with the scattering plane (i.e., the x axis as defined in Sec. II A, $\gamma = 30°$ with respect to the steps) have been marked. The Si islands on the surface were ignored. For every straight line the average surface position was calculated by linear regression; then the surface profile $\phi_3(x)$ was reconstructed and its height distribution as well as the autocorrelation function were determined. Subsequent averaging over these quantities for all profiles directly yields the rms roughness and the autocorrelation function of the interface with index 3 in Table III. Figure 13 shows the probability density function of the height distribution $p(\phi_3)$ obtained from the STM micrograph (open symbols). The fit (solid

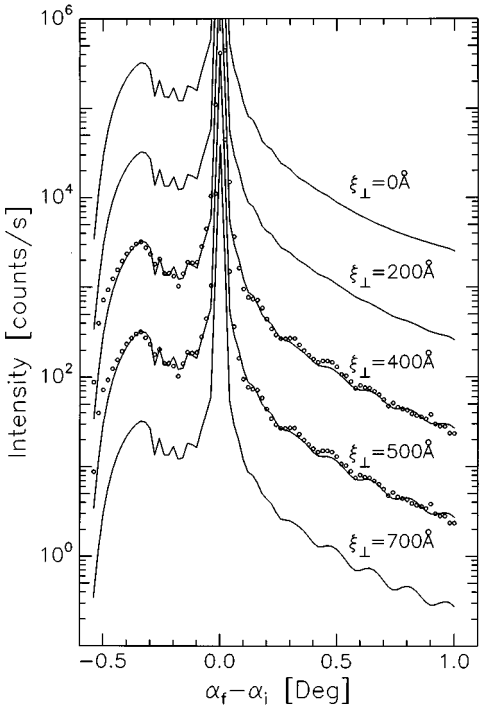

FIG. 10. Simulations (solid lines) of detector scans for $\alpha_i = 0.545°$, $\lambda = 1.540\,56$ Å, and different perpendicular correlation lengths $\xi_\perp$ together with the measurement (dotted line). The other parameters are the fit results given in Table III (second column). The curves have been shifted for clarity.

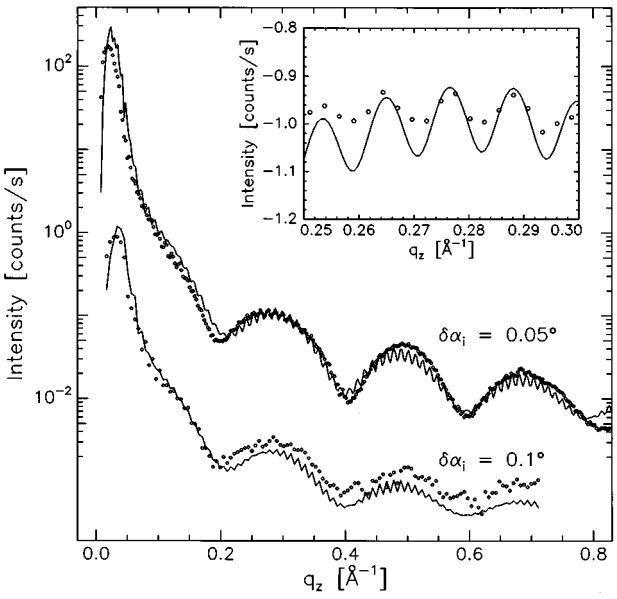

FIG. 11. Longitudinal diffuse scans carried out for two different offset angles $\delta\alpha_i$ ($\delta\alpha_i = 0.05°$, performed at the synchrotron, and $\delta\alpha_i = 0.1°$, carried out at the laboratory source). The solid lines denote the best fit and the open symbols the measurements. The inset shows an enlargement of the upper curves within the region $0.25 \leqslant q_z \leqslant 0.30$ Å^{-1}. The curves have been shifted for clarity.

line) reveals that the assumption of a Gaussian probability density function (see Sec. II B) is justified, although the interfaces exhibit a step pattern with varying terrace widths. The autocorrelation function determined by the analysis of the STM micrograph (open symbols in Fig. 14) is fitted very well with the parameters of Table II (last column) by assuming a fractal behavior of the surface [Eq. (7) in Sec. II B]. Small differences between the fit and the STM analysis can be explained by residual influences of the step periodicity:[61,62] Fig. 14 shows that (i) the difference between the fractal correlation function and that obtained with the STM is small, and (ii) the resulting difference curve is quite similar to the correlation function of a perfectly periodical step pattern. For $X > 3000$ Å the determination of the correlation function is strongly disturbed by the finite sampling interval of the STM micrograph.

One problem which was addressed at the end of Sec. II C is the one-dimensional treatment of the correlation functions. Detailed simulations using two-dimensional correlation functions were performed under the following four conditions.

(1) The step distributions in the directions parallel ($r_\parallel$) and perpendicular ($r_\perp$) to the steps have to be independent, i.e., it is allowed to factorize the cross-correlation functions.

(2) The autocorrelation function should be given by Eq. (7) for *every* direction in the interface plane.

(3) The values of the Hurst parameters must be identical for every direction in the interface plane.

(4) The ratio of the correlation lengths parallel and perpendicular to the steps has to be identical for all interfaces.

In order to show that the four above-mentioned points are valid for our particular sample we have characterized the autocorrelation function of the interface 3 in two dimensions (see Sec. II C). Therefore $C_3(|\mathbf{R}|,\gamma)$ has been determined from the STM micrograph for additional values $\gamma = 0°$, 60°, and 90°. The statistical analysis leads to the result that for all values of γ the fractal approach of Eq. (7) is justified, and within error the Hurst parameter is $h_3 \approx 0.5$ and independent of γ. Furthermore, the two-dimensional correlation function can be factorized, i.e., $C(R_\perp,R_\parallel) = C(R_\perp,0)C(0,R_\parallel)$ with $R_\perp = r'_\perp - r_\perp$ and $R_\parallel = r'_\parallel - r_\parallel$ the lateral coordinates perpendicular and parallel to the steps, respectively. In other words, the step distribution perpendicular and parallel to the steps can be assumed to be statistically independent. Figure 15 shows that the factorization of $C(R_\perp,R_\parallel)$ is justified. The position of the correlation length $\xi_3(\gamma)$ in the plane $(R_\perp,R_\parallel)$, determined by the STM analysis is marked for $\gamma = 0°$, 30°, 60°, and 90°. The error bars are given by the errors of the respective correlation length (see Table III) and the error of the angle $\gamma(\approx \pm 5°)$. The straight line in the plane $(R_\perp,R_\parallel)$ which connects the points $\xi_3(0°)$ and $\xi_3(90°)$ is the position of the correlation length $\xi_3(\gamma)$, if separability and $h_3 = 0.5$ are assumed. Because the analysis of the x-ray data shows that the epitaxially grown layers (interfaces 3–6 in Fig. 2) are correlated the shapes of the respective correlation functions should be rather similar. Thus it is reasonable to assume that the four points are valid for the lower layers, too. It turns out that the difference of the diffuse scattering calculated within a simple one- and the correct two-dimensional treatment is negligible. Finally this justifies the one-dimensional treatment of the correlation functions as done in the present work.

The densities of the evaporated layers as well as that of the substrate were set to the bulk values in the calculations.

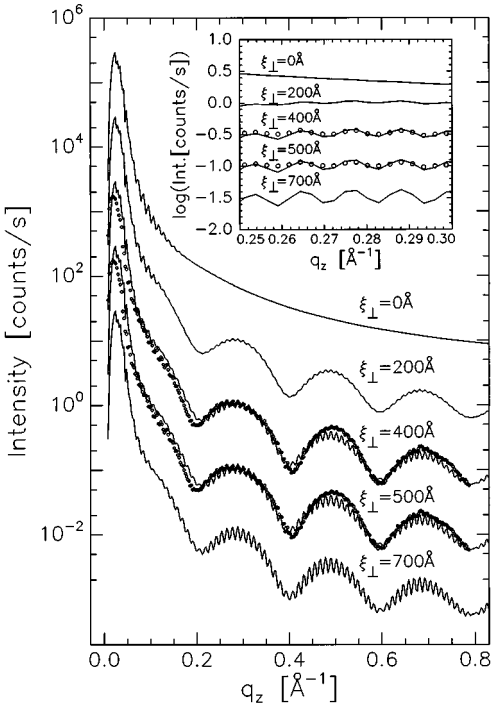

FIG. 12. Simulations (solid lines) of longitudinal diffuse scans with offset angle $\delta\alpha_i = 0.05°$ for different perpendicular correlation lengths $\xi_\perp$ together with the measurement (dotted line). The other parameters are the fit results given in Table III (second column). The inset shows an enlargement of the curves within the region $0.25 \leqslant q_z \leqslant 0.30$ Å^{-1}. The curves have been shifted for clarity.

This was done for the evaporated layers because the STM micrograph (Fig. 3) reveals a very low density of pinholes.

The x-ray results for the thicknesses of the evaporated layers (d_4, d_5, and d_6) are in very good agreement with those determined by RBS, TEM, and the quartz thickness monitor. Furthermore, the small rms roughnesses $\sigma \leqslant 2$ Å (the monolayer step height is only 3.136 Å) which were obtained by the fits of the x-ray measurements show that the buried interfaces are of very good quality.

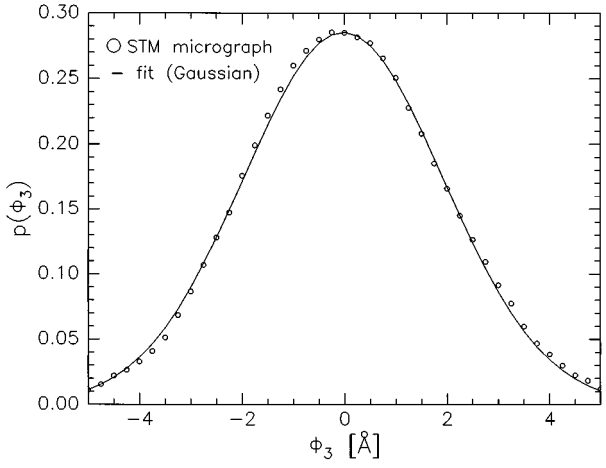

FIG. 13. Probability density function $p(\phi_3)$ of the surface heights of the upper $CoSi_2$ layer, determined by the statistical analysis of the STM micrograph shown in Fig. 3 (open symbols). The analysis procedure is explained in the text. The fit of a Gaussian is denoted by the solid line.

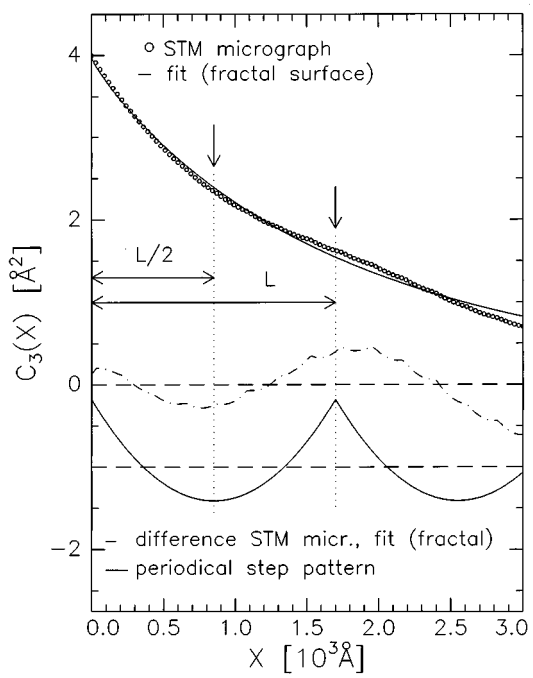

FIG. 14. Autocorrelation function $C_3(X)$ of the surface heights of the upper $CoSi_2$ layer, determined by the statistical analysis of the STM micrograph shown in Fig. 3 (open symbols). The analysis procedure is explained in the text. The fits based on a fractal model are denoted by the (upper) solid line. Additionally, the difference of the upper curves (dashed-dotted line) and the correlation function of a step structure (lowest curve, solid line) with ideal periodicity (average terrace width L) is shown. The difference curve is enlarged by a factor of 5 and the correlation function for the ideal periodical step pattern has been shifted for clarity. The arrows mark the minima and maxima of the latter curve.

Two layers on top of the $CoSi_2$/Si/$CoSi_2$ structure have to be assumed in order to get a good fit of the data. The first is an oxide layer of thickness $d_3 = 11.2$ Å and dispersion $\delta_3 = 6.5 \times 10^{-6}$. These values are reasonable for oxide layers, both of Si and of $CoSi_2$. The rms roughness of the surface of the oxide layer ($\sigma_2 = 4.4$ Å) is only slightly larger than that of the lower interfaces. The introduction of this layer improves the quality of the fit of the specular reflectivity significantly. The round shape of the Yoneda wings in the detector scans as well as their positions in the longitudinal diffuse scans reveal the existence of a critical angle of total external reflection $\alpha_c < \alpha_{c,\mathrm{Si}}$ and thus require an additional film on top of this layer. The rms roughness of this film ($\sigma_1 = 34.3$ Å) and its thickness ($d_2 = 34.4$ Å) agree within error and the electron density is very low ($\delta_2 = 3.0 \times 10^{-6}$ for $\lambda = 1.540\,56$ Å). As already mentioned, the STM micrograph (Fig. 3) shows Si islands of average height of ≈ 35 Å, which cover approximately 5% of the surface of the sample (see Sec. III). The height of these islands is identical with the thickness of this surface film. The electron density, which is much lower than the theoretical values of a Si or an oxide layer, can be explained as follows. Within the model used in this paper the islands are described by a homogeneous layer with rough interfaces.[63,64] In order to obtain a good fit, the

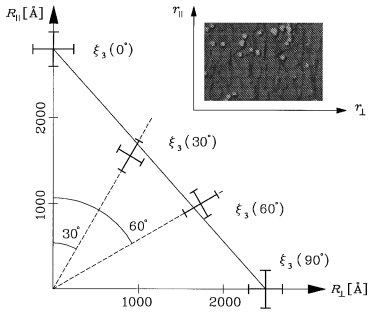

FIG. 15. Positions of the correlation lengths $\xi_3(\gamma)$ of the upper $CoSi_2$ layer surface (with error bars) for different values $\gamma=0°$, 30°, 60°, and 90° in the $(R_\perp, R_\parallel)$ plane, determined by the statistical analysis of the STM micrograph shown in Fig. 3. If the step distributions in the direction perpendicular $(r_\perp)$ and parallel $(r_\parallel)$ to the steps are assumed to be independent and $h_3=0.5$, $\xi_3(\gamma)$ is given by the straight line which connects the points $\xi(0°)$ and $\xi(90°)$. The inset shows a cut of Fig. 3 and illustrates the direction of the $r_\perp$ axis and the $r_\parallel$ axis with respect to the steps.

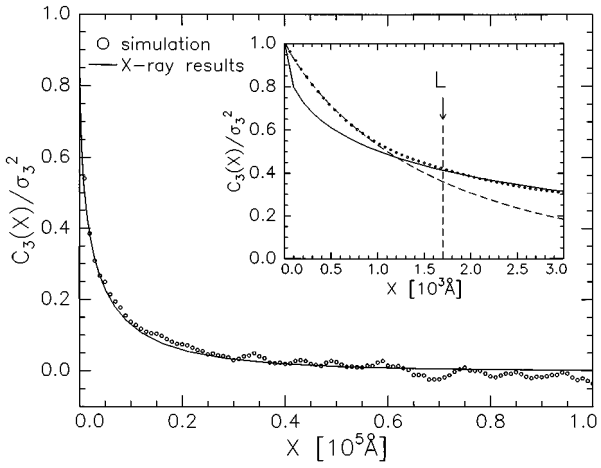

FIG. 16. Autocorrelation function $C_3(X)$ of the surface heights of the upper $CoSi_2$ layer, determined by the analysis of a simulated (stepped) interface according to the x-ray results (dotted line) and the fractal correlation function with the parameters of the x-ray analysis (solid line). L denotes the average terrace width. The inset shows that the correlation function of the simulation can be reproduced within the range $0<X<L/2$ by a fractal correlation function with $h=0.45$ (dashed line), which is the Hurst parameter determined by the STM micrograph analysis. The correlation functions are normalized to the respective squares of the rms roughness σ_3.

strong diffuse scattering from the islands is simulated by a very rough surface ($\sigma_1=34.3$ Å). Due to this large rms roughness, the electron density profile is smeared out, so that the *effective* electron density for the island layer is much lower ($\approx 1.5\times10^{-6}$) and at least of the order of the value given by the island coverage ($\approx 0.4\times10^{-6}$).

Figure 6 shows the true specular reflectivity after subtraction of the longitudinal diffuse scan with offset $\delta\alpha_i=0.05°$ (lower curve, marked by crosses) together with the fit (lower solid line). The fit results are given in the third column of Table III. Note that in contrast to the analysis of the diffuse scattering for the fit of the true specular reflectivity the introduction of an island layer is not necessary here. Furthermore, the rms roughness of the surface of the oxide layer ($\sigma_2=8.7$ Å) is much larger than the value obtained by the simultaneous analysis of all scans ($\sigma_2=4.4$ Å). The rms roughnesses and thicknesses of the epitaxial layers as well as the thickness of the oxide layer and the rms roughness of its lower interface (thicknesses and rms roughnesses 3–6) are nearly the same within error for both methods of analysis. This fact can be explained as follows for the present sample. The true specular reflectivity is mainly influenced by the parameters of the epitaxial layers and the oxide, because the interfaces are rather smooth. The surface film with low electron density is very rough and therefore the respective true specular part of the scattered radiation decays very fast with increasing q_z. In contrast to this fact, the island layer strongly influences the diffuse scattering due to its large rms roughness. Thus this layer must be introduced in the analysis which includes the diffuse scans. Although the separate fit of the true specular reflectivity is much better than the best fit which can be achieved by the simultaneous analysis of all scans, the diffuse scattering yields the more reliable set of parameters.

The diffuse scattering yields further information about the lateral structure of the roughness shapes and particularly about their correlations. The fit result of the perpendicular correlation length is $\xi_\perp=450$ Å and therefore of the order of the Si layer thickness, as already estimated by discussing qualitatively the shapes of the detector scans and longitudinal diffuse scans (see Sec. V B). The amplitudes of the fits of the longitudinal diffuse scans are slightly too large, whereas the detector scans always exhibit smaller amplitudes than the measurements (see Figs. 9 and 11). Analyzing all scans simultaneously, the best-fit result for the perpendicular correlation length $\xi_\perp=450$ Å represents a compromise which leads to rather good fits for the longitudinal diffuse scans as well as for the detector scans. In order to reduce the number of fit parameters, it was assumed that the lateral correlation lengths and the Hurst parameters are identical for interfaces of the same $CoSi_2$ layer ($\xi_3=\xi_4$, $\xi_5=\xi_6$, $h_3=h_4$, $h_5=h_6$). This is justified, because the shape of these interfaces should be very similar due to the small thicknesses of the $CoSi_2$ and the rather large perpendicular correlation length $\xi_\perp$. The in-plane correlation length $\xi_3=2200$ Å for the surface of the upper $CoSi_2$ layer (interface 3) is in very good agreement with the value $\xi_3=1800$ Å obtained by the analysis of the STM micrograph. Both values are identical within the error bars. The difference between the respective Hurst parameters $h_3=0.24$ for the x-ray measurements and $h_3=0.45$ for the STM analysis can be understood in the following way. Figure 16 shows the correlation function, obtained by the statistical analysis of a simulation of interface 3 (open symbols). This simulation has been performed in order to obtain a realization of the interface which exhibits the statistical quantities determined by the x-ray analysis ($\xi_3=2200$ Å, $h_3=0.24$). Meandering steps in contrast to a fractal shape have been explicitly included in the simulations. The spatial range covered by this x-ray experiment is approximately 200 Å$<X<10$ μm (given by the maximum q_z range of the measurements and the resolution of the instrument). In this range, the correlation function of the simu-

lated interface is very similar to that based on a fractal model and calculated with the parameters of the x-ray analysis (solid line). The inset shows the part of the simulated correlation function (open symbols) within the range $0<X<3000$ Å, which is accessible to the analysis of the STM micrograph (Fig. 3). In this range the difference between the simulation and the x-ray result is considerable. The X values are of the order of the average step distance $L=1700$ Å and the correlation function within this region is therefore dominated by the stepped nature of the interface. However, for small X values ($X<L/2$) the simulated correlation function can be reproduced by a fractal correlation function with $h=0.45$ (dashed line), which is the Hurst parameter determined by the STM micrograph. Therefore the difference between the Hurst parameters obtained by this x-ray analysis and by the STM micrograph largely seems to be caused by the different range of spatial roughness frequencies which is accessible to the two probes.

Note that the correlation functions shown in Fig. 16 are normalized to the square of the rms roughnesses $\sigma_3^2=C_3(0)$. The reconstruction of an explicitly stepped interface involves that the lateral (x) and perpendicular (z) coordinates of the local surface position are not independent of each other. Consequently, the rms roughness σ_3, which is a perpendicular length scale, cannot be chosen independently from the lateral length scale given by the correlation length ξ_3. In order to obtain the simulated interface 3 with values h_3 and ξ_3 of the x-ray analysis (see Table III), a rms roughness $\sigma_3=2.0$ Å has to be chosen. This value differs significantly from that obtained by the x-ray analysis $\sigma_3=0.9$ Å, which is just the rms roughness of a perfectly periodical pattern of monolayer steps. However, interface 3 shows meandering steps and the step distances vary, which leads to larger rms roughnesses $\sigma>0.9$ Å. Therefore it is assumed that the rms roughness $\sigma_3=0.9$ Å determined by the x-ray analysis is slightly too small and the value of the simulation ($\sigma_3=2.0$ Å) is more reasonable.

The Hurst parameter of the oxide surface layer $h_2=0.12$ is smaller compared with the lower interfaces, whereas the correlation length $\xi_2=800\pm500$ Å does not change significantly within the rather large errors: high spatial frequencies obviously dominate the shape of the oxide surface. The roughness shape of the surface film is characterized by a very large correlation length $\xi_1=27\,000$ Å (which is of the order of the distance between the Si islands) and a small Hurst parameter $h_1=0.15$, corresponding to a very jagged surface of the sample.

Figure 2 shows the real structure of the sample. With the term ''real structure'' we want to express that the interfaces are calculated using the statistical properties (i.e., correlation functions) as obtained from the x-ray analysis and the discussion above. Note that the step structure is also included in this picture. In contrast to techniques like STM and TEM which yield local information about the interfaces, Fig. 2 represents the average *global* structure because nearly the whole surface contributes to the x-ray scattering signal.

VI. SUMMARY AND CONCLUSIONS

Very good agreement between the measurements of the diffuse scattering in the range of total external reflection and the calculations following the concept of the DWBA, recently published by Holý *et al.*,[35] has been achieved. In particular, the simultaneous analysis of all scans instead of fitting the individual scans separately yields a maximum of information and increases the accuracy of the determined interface parameters, which describe the lateral as well as the vertical correlations of the interface shapes. It has turned out that the quantitative analysis of the x-ray data of this layer system is rather complex. Contributions of several interfaces are superimposed in the diffuse scattering. Furthermore, the present MBE sample is rather perfect and exhibits small roughnesses. Thus the error bars of the lateral roughness parameters ξ_j and h_j and those of the small rms roughnesses σ_j are rather large. Obviously, the determination of these parameters by analysis of the diffuse scattering reaches its limits for this particular sample. Nevertheless, a consistent and complete picture of the layer structure is obtained which is in very good agreement with other techniques. Strong conformal roughness of the adjacent interfaces within each $CoSi_2$ layer was found, whereas the interfaces of the buried Si layer are only partially correlated. The x-ray analysis shows that for the present sample the detector scans are more sensitive to the perpendicular correlation length than the longitudinal diffuse scans. Although the diffuse intensity is dominated by the very rough topmost layer, the roughness shapes of all buried interfaces of the epitaxial layers could be determined rather exactly, which is confirmed by comparison with a STM micrograph. The errors of these parameters are comparable with the errors determined by the rms roughnesses of these layers, but significantly larger than those of the thicknesses. The STM analysis reveals that for the present sample it is convenient to describe the stepped interfaces with varying terrace width by a Gaussian probability density function of the interface heights and fractal correlation functions. It is shown that the different spatial range accessible to the STM and x-ray analysis, respectively, leads to different results for the Hurst parameter of the upper $CoSi_2$ surface. Furthermore, the STM micrograph shows that the step distributions parallel and perpendicular to the average step direction could be assumed to be independent. Therefore the numerical work for the analysis of the diffuse intensity could be significantly reduced. However, the treatment of the case of nonseparable two-dimensional (auto- and cross-) correlation functions seems still to be impossible because of the enormous CPU times. The present sample is of very high quality, as shown by the x-ray analysis, which averages over the large illuminated area. Local methods like TEM and STM confirm this picture down to atomic length scales. The rms roughness is in the range of monolayer step heights. Furthermore, the step structure of the substrate is partially reproduced by the interfaces of the epitaxial $CoSi_2$/Si/$CoSi_2$ structure, because these interfaces are correlated. This means that the crystal structure is rather perfect. Thus the *template* technique allows the preparation of extremely high-quality MBE $CoSi_2$ layers with properties required by microelectronic applications.

ACKNOWLEDGMENTS

This work was supported by the Bundesministerium für Forschung und Technolgie under Grant No. 05FKABB/B.4-D01. The authors want to thank P. Müller-Buschbaum, V.

Nitz, J.-P. Schlomka, and A. Doerr for very useful discussions. The STM micrograph was taken by H. Sirringhaus, and the TEM micrographs by H. R. Deller (all at ETH Hönggerberg, Zürich, Switzerland).

*Present address: Mineralogisch-Petrographisches Institut, Universität Hamburg, Grindelallee 48, 20146 Hamburg.

[1] D. E. Savage, J. Kleiner, N. Schimke, Y.-H. Phang, T. Jankowski, J. Jacobs, R. Kariotis, and M. G. Lagally, J. Appl. Phys. **69**, 1411 (1991).

[2] Y. H. Phang, R. Kariotis, D. E. Savage, and M. G. Lagally, J. Appl. Phys. **72**, 4627 (1992).

[3] D. G. Stearns, J. Appl. Phys. **71**, 4286 (1992).

[4] D. E. Savage, Y.-H. Phang, J. J. Rownd, J. F. MacKay, and M. G. Lagally, J. Appl. Phys. **74**, 6158 (1993).

[5] A. P. Payne and B. M. Clemens, Phys. Rev. B **47**, 2289 (1993).

[6] E. E. Fullerton, J. Pearson, C. H. Sowers, S. D. Bader, X. Z. Wu, and S. K. Sinha, Phys. Rev. B **48**, 17 432 (1993).

[7] Z. H. Ming, A. Krol, Y. L. Soo, Y. H. Kao, J. S. Park, and K. L. Wang, Phys. Rev. B **47**, 16 373 (1993).

[8] Y. H. Phang, D. E. Savage, R. Kariotis, and M. G. Lagally, J. Appl. Phys. **74**, 3181 (1993).

[9] E. Spiller, D. Stearns, and M. Krumrey, J. Appl. Phys. **74**, 107 (1993).

[10] S. K. Sinha, M. K. Sanyal, S. K. Satija, C. F. Majkrzak, D. A. Neumann, H. Homma, S. Szpala, A. Gibaud, and H. Morkoc, Physica B **198**, 72 (1994).

[11] J. D. Shindler, E. A. L. Mol, A. Shalaginov, and W. H. de Jeu, Phys. Rev. Lett. **74**, 722 (1995).

[12] D. E. Savage, N. Schimke, Y.-H. Phang, and M. G. Lagally, J. Appl. Phys. **71**, 3283 (1992).

[13] D. Calecki and G. Fishman, Surf. Sci. **229**, 110 (1990).

[14] G. Fishman and D. Calecki, Phys. Rev. B **43**, 11 581 (1991).

[15] M. Kardar, G. Parisi, and Y.-C. Zhang, Phys. Rev. Lett. **56**, 889 (1986).

[16] P. Meakin, P. Ramanlal, L. M. Sander, and R. C. Ball, Phys. Rev. A **34**, 5091 (1986).

[17] D. E. Wolf and J. Villain, Europhys. Lett. **13**, 389 (1990).

[18] Z.-W. Lai and S. Das Sarma, Phys. Rev. Lett. **66**, 2348 (1991).

[19] J. Villain, J. Phys. (France) I **1**, 19 (1991).

[20] D. A. Kessler, H. Levine, and L. M. Sander, Phys. Rev. Lett. **69**, 100 (1992).

[21] H. Yan, Phys. Rev. Lett. **68**, 3048 (1992).

[22] C. Thompson, G. Palasantzas, Y. P. Feng, S. K. Sinha, and J. Krim, Phys. Rev. B **49**, 4902 (1994).

[23] D. K. G. de Boer, Phys. Rev. B **49**, 5817 (1994).

[24] D. K. G. de Boer, A. J. G. Leenaers, and W. W. van den Hoogenhof, J. Phys. (France) III **4**, 1559 (1994).

[25] In the papers of de Boer (Refs. 23 and 24) the specular reflectivity is calculated by using the second-order distorted-wave Born approximation. The resulting expression for the reflectivity now depends not only on the rms roughness, but also on the lateral structure of the rough interface.

[26] L. G. Parrat, Phys. Rev. **95**, 359 (1954).

[27] M. Born and E. Wolf, *Principles of Optics*, 2nd ed. (Pergamon, Oxford, 1964).

[28] L. Névot and P. Croce, Rev. Phys. Appl. **15**, 761 (1980).

[29] B. Vidal and P. Vincent, Appl. Opt. **23**, 1794 (1984).

[30] J. Lekner, *Theory of Reflection* (Nijhoff, Dordrecht, 1987).

[31] J. Lekner, Physica B **173**, 99 (1991).

[32] S. K. Sinha, E. B. Sirota, S. Garoff, and H. B. Stanley, Phys. Rev. B **38**, 2297 (1988).

[33] R. Pynn, Phys. Rev. B **45**, 602 (1992).

[34] V. Holý, J. Kuběna, I. Ohlídal, K. Lischka, and W. Plotz, Phys. Rev. B **47**, 15 896 (1993).

[35] V. Holý and T. Baumbach, Phys. Rev. B **49**, 10 668 (1994).

[36] D. Bahr, W. Press, R. Jebasinski, and S. Mantl, Phys. Rev. B **47**, 4385 (1993).

[37] J.-P. Schlomka, M. Tolan, L. Schwalowsky, O. H. Seeck, J. Stettner, and W. Press, Phys. Rev. B **51**, 2311 (1995).

[38] A. V. Andreev, A. G. Michette, and A. Renwick, J. Mod. Opt. **35**, 1667 (1988).

[39] W. A. Hamilton and R. Pynn, Physica B **173**, 71 (1991).

[40] A. Messiah, *Quantenmechanik*, 2nd ed. (de Gruyter, Berlin, 1985), Chap. 2.

[41] M. K. Sanyal, S. K. Sinha, A. Gibaud, S. K. Satija, C. F. Majkrzak, and H. Homa in *Surface X-Ray and Neutron Scattering*, edited by H. Zabel and I. K. Robinson, Springer Proceedings in Physics Vol. 61 (Springer-Verlag, Berlin, 1992), pp. 91–94.

[42] B. B. Mandelbrot, *The Fractal Geometry of Nature* (Freeman, New York 1982).

[43] M. F. Barnsley, R. L. Devaney, B. B. Mandelbrot, H.-O. Peitgen, D. Saupe, and R. F. Voss, *The Science of Fractal Images* (Springer-Verlag, Berlin, 1988).

[44] G. Palasantzas and J. Krim, Phys. Rev. B **48**, 2873 (1993).

[45] Following Spiller, Stearns, and Krumrey (Ref. 9), the roughness spectrum of every interface k consists of two additive components. The first describes the roughness replicated from the underlying surfaces and is given by the expression on the right-hand side of Eq. (8). The second contribution $\tilde{\phi}_k^{\mathrm{int}}(q_x)$ accounts for the intrinsic roughness of the interface k which is the roughness component introduced solely by the growth of this interface. If the interface j is assumed to be perfectly smooth, the roughness spectrum of interface k equals the term $\tilde{\phi}_k^{\mathrm{int}}(q_x)$. In our work this contribution is set to zero. Because fractal correlation functions have been assumed [Eq. (7)], it can be excluded for all spatial frequencies q_x and all interfaces j that the function $|\tilde{\phi}_j(q_x)|$ equals zero. Thus every change in the roughness spectrum from layer j to k can be completely represented by the term $\chi_{jk}\tilde{\phi}_j(q_x)$.

[46] S. F. Edwards and D. R. Wilkinson, Proc. R. Soc. London Ser. A **381**, 17 (1981).

[47] A. M. Yaglom, *Correlation Theory of Stationary and Related Random Functions* (Springer-Verlag, New York, 1987).

[48] M. K. Sanyal, S. K. Sinha, A. Gibaud, S. K. Satija, C. F. Majkrzak, and H. Homa, in *Interface Dynamics and Growth*, edited by K. S. Liang, M. P. Anderson, R. F. Bruinsma, and G. Scoles, MRS Symposia Proceedings No. 237 (Materials Research Society, Pittsburgh, 1992), p. 393.

[49] R. T. Tung, J. M. Gibson, and J. M. Poate, Phys. Rev. Lett. **50**, 429 (1983).

[50] H. v. Känel, Mater. Sci. Rep. **8**, 193 (1992).

[51] M. Müller, D. Bahr, W. Press, R. Jebasinski, and S. Mantl, J. Appl. Phys. **74**, 1590 (1993).

[52] D. Bahr, W. Press, R. Jebasinski, and S. Mantl, Phys. Rev. B **51**, 12 223 (1995).
[53] R. Feidenhans'l, Surf. Sci. Rep. **10**, 105 (1989).
[54] A. Gibaud, G. Vignaud, and S. K. Sinha, Acta Crystallogr. Sect. A **49**, 642 (1993).
[55] S. K. Sinha, J. Phys. (France) III **4**, 1543 (1994).
[56] S. R. Andrews and R. A. Cowley, J. Phys. C **18**, 6427 (1985).
[57] I. K. Robinson, Phys. Rev. B **33**, 3830 (1986).
[58] For the measurements carried out at the rotating anode the angle between the x axis and the steps was 90°. However, additional measurements performed for various sample orientations in the respective (q_x, q_z) region show no significant influence of the orientation of the diffuse scattering.
[59] Y. Yoneda, Phys. Rev. **131**, 2010 (1963).
[60] H. Dosch, Phys. Rev. B **35**, 2137 (1987).
[61] The kinematical calculation of the diffuse scattering of stepped interfaces (considering explicitly meandering steps in contrast to a fractal shape) is performed by Sinha *et al.* (Ref. 10).
[62] The average terrace width $L = 1700$ Å has been determined by the analysis of the STM micrograph as described above. The value is in accordance with the miscut $\mu = 0.21°$ listed in Table II, if the orientation of the sample ($\gamma = 30°$) is taken into account.
[63] A kinematical calculation based on a model which explicitly includes islands is given by Sinha (Ref. 55) and Satija *et al.* (Ref. 64).
[64] S. K. Satija, S. K. Sinha, E. B. Sirota, G. J. Hughes, and T. P. Russel (unpublished).